RESEARCH ACTIVITIES

Photo-Molecular Science

We study the interaction between molecules and optical fields with its possible applications to active control of molecular functionality and reactivity. We also develop novel light sources to promote those studies. Two research facilities, the Laser Research Center for Molecular Science and the UVSOR, closely collaborate with the Department.

The core topics of the Department include ultrahigh-precision coherent control of gas- and condensed-phase molecules, high-resolution optical microscopy applied to nanomaterials, synchrotron-based spectroscopy of core-excited molecules and solid-state materials, vacuum-UV photochemistry, and the development of novel laser- and synchrotron-radiation sources.

Development of Advanced Near-Field Spectroscopy and Application to Nanometric Systems

Department of Photo-Molecular Science
Division of Photo-Molecular Science I

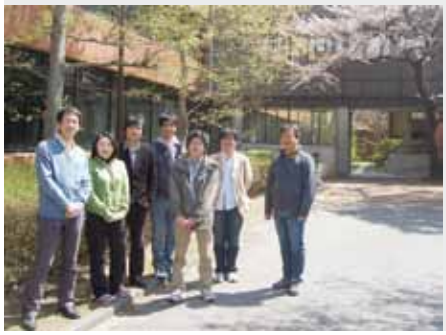

OKAMOTO, Hiromi	Professor
JEONG, Dae Hong	Visiting Associate Professor
NARUSHIMA, Tetsuya	Assistant Professor
NISHIYAMA, Yoshio	IMS Research Assistant Professor
HARADA, Yosuke	Post-Doctoral Fellow
LIM, Jong Kuk	Post-Doctoral Fellow
WU, Huijun	Graduate Student
OCHIAI, Takao	Graduate Student*
ISHIKAWA, Akiko	Technical Fellow
NOMURA, Emiko	Secretary

There is much demand for the study of local optical properties of molecular assemblies and materials, to understand mesoscopic phenomena and/or to construct optoelectronic devices in the nanometric scale. Scanning near-field optical microscopy (SNOM) is an imaging method that enables spatial resolution beyond the diffraction limit of light. Combination of this technique with various advanced spectroscopic methods may offer a direct probe of dynamical processes in nanomaterials. It may provide essential and basic knowledge for analyzing origins of characteristic features and functionalities of the nanometric systems. We have constructed apparatuses of near-field spectroscopy for excited-state studies of nanomaterials, with the feasibilities of nonlinear and time-resolved measurements. They enable near-field measurements of two-photon induced emission and femtosecond transient transmission, in addition to conventional transmission, emission, and Raman-scattering. Based on these methods, we are investigating the characteristic spatiotemporal behaviors of various metal-nanoparticle systems and molecular assemblies.

1. Visualization of Localized Optical Fields and Plasmon Wavefunctions in Metal Nanostructures

We recently reported that wavefunctions of localized plasmon resonances of chemically synthesized metal (Au and Ag) nanoparticles are visualized by near-field transmission or two-photon excitation measurements.[1)] The same methods were also applied to Au nanoparticle assemblies to visualize confined optical fields.[1)] It was revealed for the dimers that highly localized optical field is generated at the interstitial sites between the particles. In many-particle assemblies, the localized fields were especially intensified at the rim parts of the assemblies, and such a characteristic field distribution has been attributed to interaction between plasmon excitations induced on the particles.[2)]

We have extended the studies to metal nanostructures manufactured by the electron-beam lithography technique, in collaboration with researchers of other institution, or other top-down fabrication techniques, with which structures that are difficult to obtain with the chemical methods can be available. As an example, near-field properties of nano-void structures, opened on thin gold metallic films on glass substrates, were characterized, and the field distributions in the vicinities of the voids were visualized.[3)] In circular void chain structures, we found that confined optical fields were generated in the interstitial sites between voids under some circumstances (Figure 1). The field distributions were analyzed based on the electromagnetic theories and calculations. The observed and calculated field distribution was discussed in relation to Babinet's principle in optics, which gives general relation between electromagnetic field distributions for complementary nanostructures made of thin conductors, such as a nanoparticle assembly and a nano-void assembly.

Such a study is essential as a basis for designing unique optical properties and functions of metal nanostructures, and their applications to highly sensitive spectroscopic methods and exotic photochemical fields, as well as to nanoscale optical waveguids.

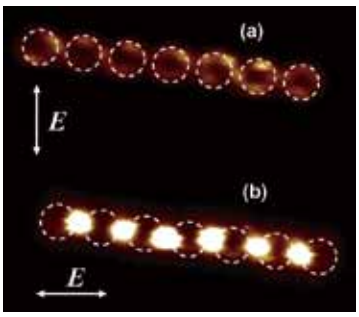

Figure 1. Near-field two-photon excitation images of a nanovoid chain opened on a Au film (thickness ~20 nm).[3)] The diameter of the void was ~400 nm. The incident polarization was nearly perpendicular (a) and parallel (b) to the chain. Excitation: 785 nm.

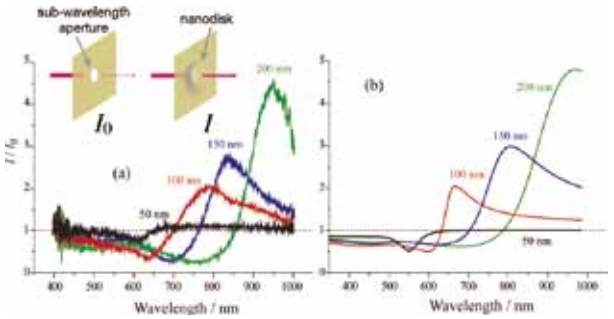

Figure 2. Transmittance spectra of capped nanoapertures, (a) experimental and (b) model calculation. The inset shows the schematic models of an uncapped and a capped nanoapertures.

2. Anomalous Light Transmission through Capped Nanoapertures

In the course of near-field studies on metal nanodisks fabricated on glass substrates by electron-beam lithography, we examined light intensity transmitted through a nanometer-scale aperture opened on an opaque metallic screen. When the aperture is obscured by an opaque metallic disk (cap) with a larger diameter than the aperture, the transmitted light was found to be, paradoxically, even stronger than that without the disk.[4)]

We investigated spectroscopic characteristics of light transmission through a nanoaperture on a gold film with a diameter of ~100 nm (Figure 2, inset, left; apertured near-field probe, in practice) and that capped with gold nanodisks (diameter 50–200 nm) at a distance of ~30 nm from the aperture (Figure 2, inset, right). The transmittance through the capped aperture is defined as the ratio between intensities for the capped aperture (I) and for the aperture without the disk (I_0) and is plotted in Figure 2(a). In the long wavelength region, the transmittance through the capped aperture exceeds 1, and surprisingly, the maximum transmittance becomes even higher for larger disks. We analyzed the spectra based upon a theoretical model, and it turned out that the phenomenon arise from the property of localized plasmon resonances: The anomalous transmission is due to highly efficient performance of the nanodisks for conversion between near-field and far-field radiations.

3. Nonlinear Effects in Optical Trapping

The optical trapping technique has been widely used in various areas to manipulate particles, cells, and so forth. The principle of trapping is based on the interaction between optical electric fields and induced linear polarizations. In the course of the studies on behavior of gold nanoparticles under pulsed laser fields, we have found a novel phenomenon of optical trapping of spherical gold nanoparticles arising from nonlinear polarization when we trap the nanoparticles by

Figure 3. Two gold nanoparticles trapped by ultrashort pulses. Two particles are trapped separately and aligned along the incident laser polarization (arrows).

ultrashort near-infrared laser pulses.[5)] That is, the stable trap site (usually appears in the center of the focused beam) is split into two equivalent positions, and the split trap positions are aligned along the direction of the incident laser polarization. The split distance depends on the trapping-laser power and wavelength. We have found that the results were successfully interpreted in terms of the nonlinear polarization caused by the femtosecond pulses. This is the first report that treats the nonlinear effects in optical trapping.

4. Construction of Apparatuses for Nonlinear and Ultrafast Near-Field Spectroscopy

In previous studies we achieved ultrafast near-field imaging with a time resolution of ~100 fs.[1)] To further extend the dynamical studies of plasmons, we are now developing an apparatus that achieves near-field time-resolved measurements with < 20 fs time resolution. We have also constructed an apparatus for near-field/far-field microscopic nonlinear optical measurements based on the technique of atomic-force microscope.

5. Near-Field Imaging of Organic Molecular Assemblies and Hybrid Systems

We are studying nanometric structures and optical properties of organic molecular assemblies such as LB films of functional conjugated molecules, and hybrid systems consist of metal nanoparticles and organic functional materials, mainly as collaborations with other research groups.

References

1) H. Okamoto and K. Imura, *Prog. Surf. Sci.* **84**, 199–229 (2009).
2) H. Okamoto, K. Imura, T. Shimada and M. Kitajima, *J. Photochem. Photobiol., A* **221**, 154–159 (2011).
3) S. I. Kim, K. Imura, S. Kim and H. Okamoto, *J. Phys. Chem. C* **115**, 1548–1555 (2011).
4) K. Imura, K. Ueno, H. Misawa and H. Okamoto, *Nano Lett.* **11**, 960–965 (2011).
5) Y. Jiang, T. Narushima and H. Okamoto, *Nat. Phys.* **6**, 1005–1009 (2010).

* carrying out graduate research on Cooperative Education Program of IMS with University of Tsukuba.

Design and Reconstruction of Molecular Quantum States of Motion

Department of Photo-Molecular Science
Division of Photo-Molecular Science I

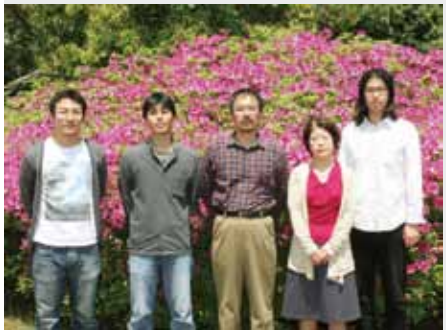

OHSHIMA, Yasuhiro	Professor
MIZUSE, Kenta	Assistant Professor
HAYASHI, Masato	Post-Doctoral Fellow
MIYAKE, Shinichiro	Graduate Student
INAGAKI, Itsuko	Secretary

Molecules are vital existence. In a gas-phase ensemble at room temperature, they are, in an average, flying away by a few hundred meters, making turns almost reaching to 10^{11} times, and shaking themselves more than 10^{13} times within the duration of only one second. The ultimate goal this research group has been aiming to is to capture the lively figures of molecules moving in such a dynamic manner and to have a perfect command over the molecular motions. Here lasers with ultimate resolution in time and energy domains are employed complementally and cooperatively for this purpose.

1. Unveiling the Nonadiabatic Rotational Excitation Process in a Symmetric-Top Molecule Induced by Two Intense Laser Pulses[1)]

When gaseous molecules are irradiated by an intense nonresonant ultrafast laser pulse, rotation of molecules is coherently excited via the interaction with the molecular anisotropic polarizability, to create a rotational quantum wave packet (WP). We has developed a method for exploring such a nonadiabatic rotational excitation (NAREX) process in a quantum-state resolved manner, and reported rotational-state distributions after the impulsive excitation with a fundamental output of a femtosecond (fs) Ti:Sapphire laser.[2,3)]

We made an extended study for unveiling the NAREX process in symmetric-top molecules. Benzene molecules have been taken as a sample. The initial state distribution was restricted mostly to the five lowest rotational levels in different nuclear-spin manifolds by an extensive adiabatic cooling with the rotational temperature well below 1 K, and distributions after the interaction with a fs double-pulse pair (3–5 TW/cm^2 each with 160 fs duration) with time delays were probed by employing resonant enhanced two-photon ionization (R2PI) *via* the $S_1 \leftarrow S_0$ 6_0^1 vibronic transition with nanosecond (ns) dye laser pulses. Populations of 10 rotational levels with J ranging from 0 to 4 and K from 0 to 3 were examined to show an oscillatory dependence on the time delay between the two pulses. Fourier analysis of the beat signals provides the coupling strengths between the constituent levels of the rotational WPs created by NAREX. These data agrees well with the results from quantum mechanical calculations, evidencing stepwise excitation pathways in the wave packet creation with $\Delta J = 2$ for $K = 0$ stack while $\Delta J = 1$ and 2 in $K > 0$ stacks.

2. Controlling the Sense of Molecular Rotation: Classical vs Quantum Analysis[4)]

The anisotropy of molecular system is represented as a non-uniform distribution of projections, M, of angular momentum, J, onto a space-fixed (Z) axis. The system is designated as being *oriented* when the populations for $+M$ and $-M$ are different. In the classical vector model, the + or – orientation corresponds to clockwise or counter-clockwise rotation, respectively. We have shown that a pair of linearly-polarized intense ultrafast pulses creates molecular ensembles with oriented rotational angular momentum, when the delay and the mutual polarization between the laser fields are appropriately arranged.[5)]

We have further undertaken a comparative study of the classical and quantum aspects of the underlying mechanism of the effect. Good quantitative agreement is found between the classical description of the process and the rigorous quantum mechanical analysis at the relevant experimental conditions. Both approaches predict the same optimal values for the delay between pulses and the angle between them, and deliver the same magnitude of the induced oriented angular momentum of the molecular ensemble. As expected, quantum and classical analysis substantially deviate when the delay between pulses is comparable with the period of quantum rotational revivals. However, time-averaged characteristics of the excited molecular ensemble are equally good described by these two approaches. This is illustrated by calculating the anisotropic time-averaged angular distribution, which reflects persistent confinement of the molecular axes to the rotation plane defined by two polarization vectors of the pulses.

3. Reconstruction of the Rotational Wave Packet Created by NAREX and Ultrafast State-Distribution Control

The fs-pump and ns-probe approach has been also adopted for a detailed study on characterization and control of the rotational WP in NO. For double fs-pulse excitation, the population of each rotational state showed oscillatory change against the time delay between the two pulses. As has been shown previously,[6] the delay dependence pertinent to the initially populated state allowed us to determine the amplitude and phase of each eigenstate that constitutes the rotational WP. The experimental results, in particular, the systematic phase shifts against J, represented a clear signature of bifurcated excitation pathways in the WP creation, which is characteristic to linear molecules in a doubly degenerate vibronic state. We have also shown that the final distribution can be concentrated into a narrow range of states if the time delay between the two pulses is properly arranged. For instance, almost 80% can be repopulated in the initial J = 1/2 state. Highly focused population has been achieved also for J = 3/2 and 5/2. The experimental finding has demonstrated the capability of state-distribution control in an ultrafast time scale (within several tens of picoseconds).

4. Coherent Intermolecular-Mode Excitation of NO–Ar by Nonresonant Intense Femtosecond Laser Fields

Nonadiabatic interactions with a nonresonant ultrafast laser field can coherently excite also molecular vibration. Here, vibrational distribution after nonadiabatic vibrational excitation (NAVEX) is probed in a quantum-state resolved manner. The method has been applied to NO–Ar. R2PI spectrum of NO–Ar associated to the monomer A–X (0,0) transition exhibited a number of hot bands when the fs pump pulse was applied. These hot band transitions are assigned to those from vibrationally excited states pertinent to intermolecular modes, of which excitation energies range in 4–30 cm^{-1}. Thus we have successfully probed the intermolecular vibrational energy levels up to 1/3 of the total binding energy of NO–Ar, which is estimated to be *ca.* 90 cm^{-1}. When the cluster was excited with a pair of fs pulses, the intensities of monitored vibronic bands changed oscillatory against the delay between the two pulses. These results indicate the creation of a quantum WP pertinent to intermolecular vibrations in the electronic ground state. Real-time WP propagation was calculated by numerically solving the time-dependent Schrödinger equation on the intermolecular potential energy surface.

5. High-Resolution Laser Spectroscopy of Benzene Clusters with He Atoms and H_2 Molecules

Molecular clusters containing benzene are prototypical systems for elucidating the intermolecular interaction pertinent to aromatic rings. We are now focusing on clusters of benzene attached by small numbers of atoms and molecules. Specifically, high-resolution electronic spectra of benzene–$(He)_n$ and –$(H_2)_n$ (n = 1, 2) have been examined via two-color R2PI in the vicinity of the monomer S_1–S_0 6_0^1 band. We employed a tripled output from a ns pulsed dye amplifier, which was injection-seeded by the CW output from a Ti:Sapphire laser, as an excitation source. Owing to the narrow band width (~250 MHz) of the laser system and the efficient rotational cooling down to 0.3 K by implementing a high-pressure pulsed valve, rotational structures have been fully resolved. The observed spectra shows unambiguously that He and H_2 are located above the center of the benzene molecular plane (for the both sides in the case of n = 2), and the H_2 molecular axes are perpendicular to the plane. The rotational constants thus determined set the distances of He and H_2 above the plane to be: 3.602 (+0.063) Å and 3.477 (+0.131) Å, respectively, where values in parentheses represent the change by the excitation from S_0 to S_1. Several vibronic bands associated to excitation of intermolecular vibrations have also been observed for all the clusters examined. The vibrational frequencies of benzene(S_1)–He are derived as: 17 and 13 cm^{-1} for the intermolecular stretch and bend modes, respectively. The values in the complex with H_2 are: 48 cm^{-1} for the stretch, while 34 and 39 cm^{-1} for the two bend modes. The vibronic bands of benzene–He exhibit tunneling splitting due to a large-amplitude migration of He above and below the benzene molecular plane. This finding is matched with the prediction based on a high-level *ab initio* calculation.

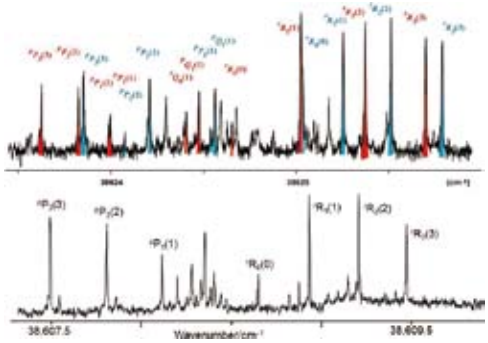

Figure 1. High-resolution excitation spectra of C_6H_6–He: (bottom) the $S_1 \leftarrow S_0$ 6_0^1 band, (top) the intermolecular-stretch excited band. Each rotational line is split into two (indicated in red and blue) due to quantum tunneling.

References

1) D. Baek, H. Hasegawa and Y. Ohshima, *J. Chem. Phys.* **134**, 224302 (10 pages) (2011).
2) H. Hasegawa and Y. Ohshima, *Phys. Rev. A* **74**, 061401 (4 pages) (2006).
3) H. Hasegawa and Y. Ohshima, *Chem. Phys. Lett.* **454**, 148–152 (2008).
4) Y. Khodorkovsky, K. Kitano, H. Hasegawa, Y. Ohshima and I. Sh. Averbukh, *Phys. Rev. A* **83**, 023423 (10 pages) (2011).
5) K. Kitano, H. Hasegawa and Y. Ohshima, *Phys. Rev. Lett.* **103**, 223002 (4 pages) (2009).
6) H. Hasegawa and Y. Ohshima, *Phys. Rev. Lett.* **101**, 053002 (4 pages) (2008).

Development of High-Precision Coherent Control and Its Applications

Department of Photo-Molecular Science
Division of Photo-Molecular Science II

OHMORI, Kenji	Professor
KATSUKI, Hiroyuki	Assistant Professor
TAKEI, Nobuyuki	Assistant Professor
GOTO, Haruka	Post-Doctoral Fellow
NAKAGAWA, Yoshihiro	Graduate Student
KOYASU, Kuniaki	Graduate Student
INAGAKI, Itsuko	Secretary
YAMAGAMI, Yukiko	Secretary

Coherent control is based on manipulation of quantum phases of wave functions. It is a basic scheme of controlling a variety of quantum systems from simple atoms to nanostructures with possible applications to novel quantum technologies such as bond-selective chemistry and quantum computation. Coherent control is thus currently one of the principal subjects of various fields of science and technology such as atomic and molecular physics, solid-state physics, quantum electronics, and information science and technology. One promising strategy to carry out coherent control is to use coherent light to modulate a matter wave with its optical phase. We have so far developed a high-precision wave-packet interferometry by stabilizing the relative quantum phase of the two molecular wave packets generated by a pair of femtosecond laser pulses on the attosecond time scale. We will apply our high-precision quantum interferometry to gas, liquid, solid, and surface systems to explore and control various quantum phenomena.

1. Strong-Laser-Induced Quantum Interference[1)]

Molecules are expected to be promising information devices. Theoretical proposals have been made for logic gates with a molecular wave packet modulated by a strong femtosecond laser pulse. However, it has not yet been observed how this changes the population of each eigenstate within the wave packet. Here we demonstrate direct observation of the population beating clearly as a function of the delay of the strong laser pulse. The period is close to the recurrence period of the wave packet, even though a single eigenstate should have no information on the wave-packet motion. This unusual beat arises from quantum interference among multiple eigenstates combined on a single eigenstate. This new concept, which we refer to as 'strong-laser-induced interference,' is not specific to molecular eigenstates, but universal to the superposition of any eigenstates in a variety of quantum systems, being a new tool for quantum logic gates, and providing a new method to manipulate wave packets with femtosecond laser pulses in general applications of coherent control.

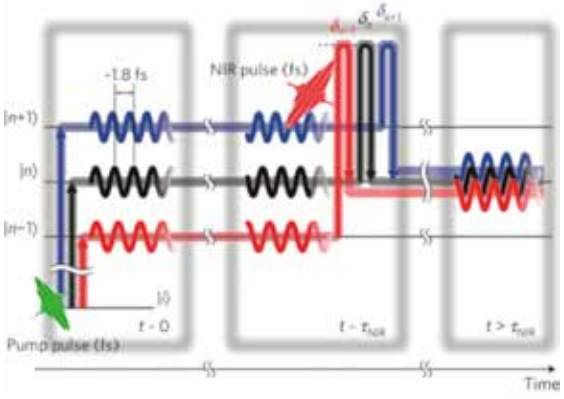

Figure 1. Starting from a common initial state *i*, there are multiple pathways given by the pump and strong near-infrared (NIR) laser pulses to the common final state *n*. Those multiple pathways interfere with each other. The amounts of phase shifts during the NIR pulse are indicated as δ_{n-1}, δ_n, and δ_{n+1}.

2. Optical Manipulation of Coherent Phonons in Superconducting $YBa_2Cu_3O_{7-\delta}$ Thin Films[2)]

The coherent phonons of $YBa_2Cu_3O_{7-\delta}$ are believed to be strongly coupled to its superconductivity. Controlling the

phonons below its transition temperature, therefore, may serve as a promising scheme of the control of superconductivity. Here we demonstrate optical manipulation of the Ba–O and Cu–O vibrations in a thin-film $YBa_2Cu_3O_{7-\delta}$ below its transition temperature using a pair of femtosecond laser pulses. The interpulse delay is tuned to integral and half-integral multiples of the oscillation period of a specific phonon mode (Ba–O or Cu–O vibration) to enhance and suppress its amplitude, respectively.

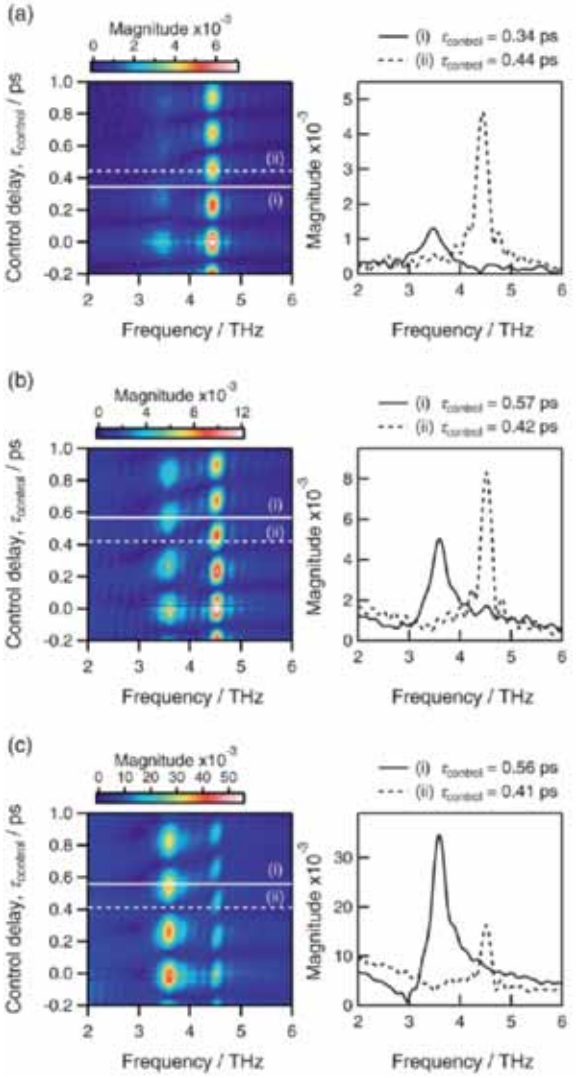

Figure 2. Fast-Fourier-transform of the temporal evolutions of the coherent phonons induced by a pair of femtosecond laser pulses in $YBa_2Cu_3O_{7-\delta}$ thin films with temperatures (a) 296 K, (b) 78 K, and (c) 8 K. They are plotted as functions of the interpulse delay $\tau_{control}$ in the left column. The right column shows cross sections along the solid (i) and broken (ii) lines in the left column at each temperature.

References

1) H. Goto, H. Katsuki, H. Ibrahim, H. Chiba and K. Ohmori, *Nat. Phys.* **7**, 383–385 (2011).
Highlighted by Nat. Phys. **7**, 373–374 (2011).
Highlighted by Nat. Photonics **5**, 382–383 (2011).
2) Y. Okano, H. Katsuki, Y. Nakagawa, H. Takahashi, K. G. Nakamura and K. Ohmori, *Faraday Discuss.* **153**, 375–382 (2011). (invited paper).

Awards

KATSUKI, Hiroyuki; The Young Scientist's Prize of The Commendation for Science and Technology by the Minister of Education, Culture, Sports, Science and Technology, Japan.
KATSUKI, Hiroyuki; MORINO Foundation research award.

Molecular Inner-Shell Spectroscopy: Local Electronic Structure and Intermolecular Interaction

Department of Photo-Molecular Science
Division of Photo-Molecular Science III

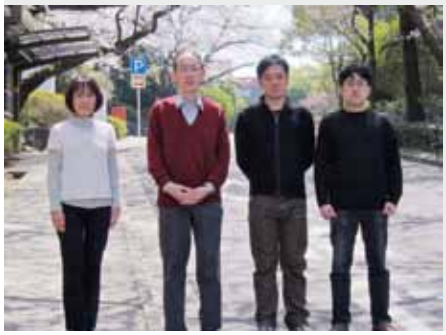

KOSUGI, Nobuhiro	Professor
YAMANE, Hiroyuki	Assistant Professor
NAGASAKA, Masanari	Assistant Professor
NAKANE, Junko	Secretary

In order to reveal local electronic structures and weak intermolecular interactions in molecular solids, liquids, and clusters, we are developing and improving several kinds of soft X-ray spectroscopic techniques such as X-ray photoelectron spectroscopy (X-ray PES, XPS), X-ray absorption spectroscopy (XAS), resonant Auger electron spectroscopy (RAS), X-ray emission spectroscopy (XES), resonant XES (RXES), and resonant inelastic X-ray scattering (RIXS), at UVSOR in-vacuum undulator beamlines BL-3U and BL-6U with some international collaboration programs, and also an original *ab initio* quantum chemical program package GSCF, which is optimized to calculation of molecular inner-shell processes.

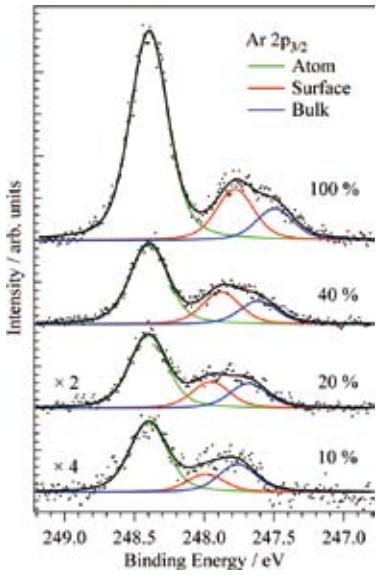

Figure 1. Ar $2p_{3/2}$ XPS spectra for mixed Ar-N_2 clusters prepared from different mixing ratio of Ar. The surface and bulk sites of the mixed clusters are separately obtained by a fitting procedures.

1. Structures of Small Mixed Ar-N_2 Clusters Studied by Soft X-Ray Photoelectron Spectroscopy[1)]

Figure 1 shows Ar $2p_{3/2}$ XPS spectra for Ar and mixed Ar-N_2 clusters of different compositions. The surface and bulk sites of the clusters are distinguished by a fitting procedure. The cluster size of 200 corresponds to icosahedral multilayer structures with 4 or 5 layers. The intensity ratio of the surface and bulk sites observed for the Ar $2p_{3/2}$ XPS spectra of the pure (100%) Ar_{200} cluster is consistent with such icosahedral multilayer structures. On the other hand, in 10% Ar, the intensity of the surface sites is smaller than that of the bulk sites. This intensity ratio suggests a core-shell structure, where the Ar aggregates are located in the bulk and are covered by a N_2 shell. We have roughly estimated the composition of N_2 bound in clusters from the partial pressure of N_2, and confirmed that the surface-to-bulk ratio of Ar is consistent with a core-shell structure, where Ar is covered by N_2. These core-shell structures are also observed in expansions containing 20 and 40% Ar.

2. Electronic Structure of Liquid Methanol Studied by Carbon K-Edge Soft X-Ray Absorption Spectroscopy[2)]

Figure 2 shows C K-edge XAS spectra of molecular (gas) and liquid methanol at 25 °C. Two peaks around 288 and 289.5 eV and several Rydberg states are observed in the molecular spectra. The 288 eV and 289.5 eV peaks contain O–H and C–H components, respectively, and the 292.5 eV peak contains a σ* C–O component. Our C K-edge XAS spectrum of liquid methanol shows a simple structure with three contributions around 288.5, 290, and 293 eV as shown in

Figure 2(b).

The peak around 288.5 eV in liquid methanol is shifted to higher photon energy compared to that of methanol gas. The energy shift (0.53 eV) would be caused by the formation of the hydrogen bonding networks between methanol molecules. The peak around 290 eV in liquid methanol is also shifted to higher photon energy, but the energy shift (0.20 eV) is smaller than in the first band. This may be explained by a dominant contribution from the hydrophilic OH component in the first band. The peak around 293 eV does not show a noticeable difference between gas and liquid because the σ* (C–O) orbital is not influenced by the hydrogen bonding network.

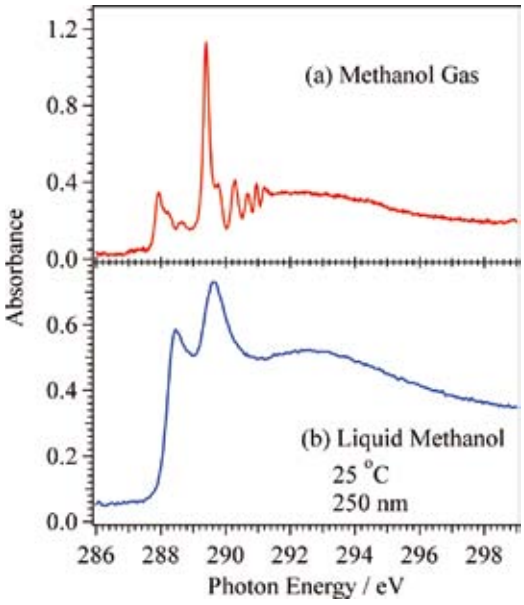

Figure 2. Carbon K-edge XAS spectra for (a) methanol gas and (b) liquid methanol at 25 °C. The thickness of liquid methanol layer is estimated to be 250 nm.

3. Very Narrow Intermolecular Electronic Band Dispersion in a Crystalline Film of Zn-Phthalocyanine[3)]

The electronic band dispersion, energy *versus* wave vector: $E(\boldsymbol{k})$, is a fundamental parameter to understand electric properties of solids such as hole mobility (μ_h). In the field of organic semiconductors, study of the intermolecular $E(\boldsymbol{k})$ shows a rapid progress due to the needs of the interpretation of the charge transport mechanism in molecular electronic devices. However, due to very weak intermolecular interaction and difficulty in preparing crystallized films appropriate for the $E(\boldsymbol{k})$ measurement, the observation of the intermolecular $E(\boldsymbol{k})$ has been limited in the case of high-μ_h materials. In order to elucidate and control the functionality of organic semiconductors, a systematic and quantitative experiment on the intermolecular interaction is essential. In this work, we have succeeded to observe a very narrow intermolecular $E(\boldsymbol{k})$ in crystalline films of Zn-phthalocyanine (ZnPc), which is one of the promising materials in the field of organic electronics.

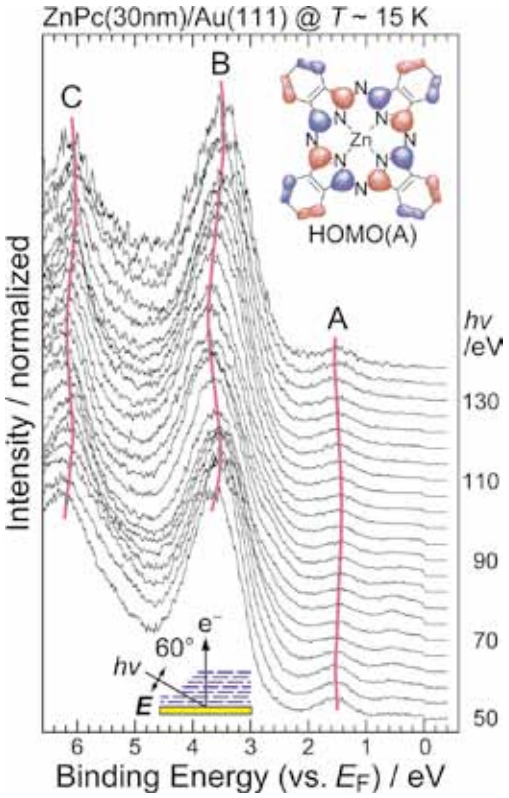

Figure 3. The *h*ν dependent angle-resolved PES spectra (4 eV step) at the normal emission for the crystalline ZnPc films on Au(111) at 15K.

Figure 3 shows *h*ν dependent angle-resolved PES (ARPES) spectra at the normal emission for the ZnPc crystalline film on Au(111) at 15 K. Since the ZnPc crystalline film on Au(111) shows a Stranski-Krastanov growth mode, there are the remanent substrate signal such as a Fermi edge, which we can use for the fine *h*ν calibration. For the ZnPc-derived peaks A, B, and C, we have observed a clear dispersive behavior with *h*ν, wherein (i) the periodicities of A–C are the same in the $\boldsymbol{k}$ space and (ii) the bandwidth of peak A, originating from the highest occupied molecular orbital (HOMO), is 120 meV.

The present observation clearly indicates that the band-like transport is realized in the phthalocyanine films by the control of the geometric film structure. Moreover, the present result can be a benchmark for the systematic study on the intermolecular interaction, *e.g.*, intermolecular $E(\boldsymbol{k})$ as a function of the central metal atom in the phthalocyanine molecule, which enables to discuss experimentally the intermolecular interaction in terms of the intermolecular distance and the molecular orbital symmetry.

References

1) M. Nagasaka, E. Serdaroglu, R. Flesch, E. Rühl and N. Kosugi, to be published.
2) M. Nagasaka and N. Kosugi, to be published.
3) H. Yamane and N. Kosugi, to be published.

Photoabsorption and Photoionization Studies of Fullerenes and Development of High-Efficiency Organic Solar Cells

Department of Photo-Molecular Science
Division of Photo-Molecular Science III

MITSUKE, Koichiro	Associate Professor
KATAYANAGI, Hideki	Assistant Professor
LE, Hong Quang	Post-Doctoral Fellow
PRAJONGTAT, Pongthep	Research Fellow
MORENOS, Lei Angeli S.	Visiting Scientist
BASHYAL, Deepak	Graduate Student
ASARI, Chie	Technical Fellow
SHIMIZU, Atsuko	Secretary

We have observed the formation of multiply-charged photoions from gaseous fullerenes or aromatic hydrocarbons irradiated with synchrotron radiation at $h\nu$ = 25 to 200 eV. We thus studied the mechanisms and kinetics of consecutive C_2-release reactions on the basis of (i) the yield curves for the fragments $C_{60(70)-2n}^{z+}$ ($n \geq 1$, z = 1–3) as a function of the primary internal energy and (ii) the three dimensional velocity distributions of the fragments. Last year the velocity distributions of C_{60-2n}^{z+} and C_{70-2n}^{z+} were measured for the first time. Concepts of the microcanonical temperature and Arrhenius-type rate constants for individual C_2 ejection steps allowed us to compare the experimental total average kinetic energy with theoretical kinetic energy release predicted from the "model free approach" developed by Klots.

In the second topic we have fabricated dye-sensitized solar cells (DSSCs) containing ruthenium dye and iodide electrolyte and measured their short-circuit current and the intensity of the transmitted light to estimate the wavelength dependence of the incidence photon-to-current conversion efficiency (IPCE) and photoabsorbance (ABS) in the range of 300 to 1000 nm. In addition, we evaluated the quantum yield (APCE) of DSSCs for the electron injection from the excited orbital of Ru dye to the conduction band of TiO_2 nanoparticles. Our final goal is to develop DSSCs with high performance and long lifetime by improving ABS and APCE mainly in the near infrared region.

1. Mass-Analyzed Velocity Map Imaging of Photofragments from C_{70}[1)]

The velocity distributions of the fragments produced by dissociative photoionization of C_{70} have been measured at several photon energies in the extreme UV region, by using a flight-time resolved velocity map imaging (VMI) technique combined with a high-temperature molecular beam and synchrotron radiation. Average kinetic energy release was estimated for the six reaction steps of consecutive C_2 emission, starting from $C_{70}^{2+} \rightarrow C_{68}^{2+} + C_2$ to $C_{60}^{2+} \rightarrow C_{58}^{2+} + C_2$. The total kinetic energy generated in each step shows a general tendency to increase with increasing $h\nu$, except for the first and fifth steps. This propensity reflects statistical redistributions of the excess energy in the transition states for the above fragmentation mechanism. Analysis based on the finite-heat-bath theory predicts the detectable minimum cluster sizes at the end of the C_2–emission decay chain. They accord well with the minimum sizes of the observed ions, if the excess energy in the primary C_{70}^{2+} is assumed to be smaller by ~15 eV than the maximum available energy. The present VMI experiments reveal remarkably small kinetic energy release in the fifth step, in contradiction to theoretical predictions, which suggests involvement of other fragmentation mechanisms in the formation of C_{60}^{2+}.

2. Velocity Map Imaging for Photoionization of Polycyclic Aromatic Hydrocarbons

We have demonstrated the versatility of our apparatus in photoionization study of various nonvolatile substances, by taking an example of complicated dissociation of sumanene $C_{21}H_{12}$ and coronene $C_{24}H_{12}$ in the extreme UV. Though their chemical reactions are sometimes discussed by analogy with those of C_{60}, a great difference in the velocity distribution has been observed between the fragment ions from C_{60} and those from sumanene. The appearance $h\nu$ values for C_{60-2n}^{z+} are higher by 30–33 eV than their thermochemical thresholds for dissociative ionization of C_{60}. Usually, the relative abundance of C_{60-2n}^{z+} is two orders of magnitude lower than that of the parent C_{60}^{z+}. In contrast, the y–t map of sumanene in Figure 1 suggests prompt coulomb explosion of $C_{21}H_{12}^{z+}$ (z = 2 and 3) into singly-charged fragments followed by stepwise C_2 ejection. This argument appears to hold true in the case of photodissociation of coronene $C_{24}H_{12}$.

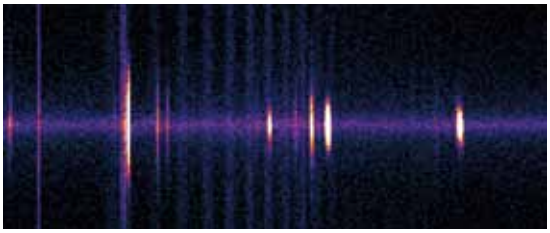

Figure 1. Map of *y*–*t* of the photoions from $C_{21}H_{12}$. The *y* and *t* coordinates are proportional to the *y* component of the ion velocity and the square root of mass-to-charge ratio *m*/*z*, respectively.

3. Photoexcitation and Electron Injection Processes in Azo Dyes Adsorbed on Nanocrystalline TiO_2 Films[3)]

Dye-sensitized solar cells were fabricated using eight azo dyes which have different positions and/or numbers of carboxyl and hydroxyl groups. The short-circuit current density, photoabsorbance, absorptance and quantum yield for dyes-to-TiO_2 electron injection were measured by photons ranging from 380 to 800 nm. X-ray and ultraviolet photoelectron spectroscopy of the photovoltaic electrodes were also conducted. The photon-to-current conversion efficiency of the cells was found to depend mostly on the relative position of the lowest unoccupied molecular orbital of the adsorbed dyes and partly by their concentration on the TiO_2 nanoparticles.

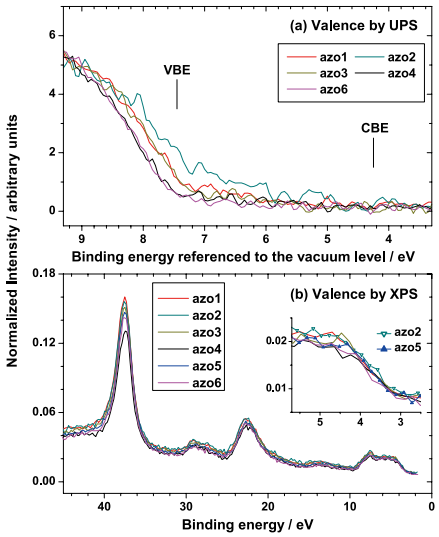

Figure 2. Ionization of valence and Ti 3p electrons of the TiO_2 film covered with six azo dyes on the working electrodes observed by photoelectron spectroscopy.

4. Efficient Dye-Sensitized Solar Cells Made from TiO_2 Nanoparticles Powder, VP P90[4)]

Dye sensitized solar cells (DSSCs) were fabricated by means of a wet process using the paste of titanium dioxide (TiO_2) prepared from commercial powders of TiO_2 nanopartilces, VP TiO_2 P90 and AEROXIDE® TiO_2 P25. The other ingredients of the TiO_2 pastes were ethanol, aqueous solution of acetic acid, α-terpineol, and ethyl cellulose. The optimum composition has been determined by comparing the energy conversion efficiencies of assembled DSSCs. The sensitizer dye is the Ruthenium 535-bisTBA in acetonitrile solution. The conversion efficiency of 9% or higher has been obtained by using a double-layer film of P90-type TiO_2 with an immersion of FTO glass into a $TiCl_4$ solution and an additional coating of a light scattering layer.

5. Fabrication, Analysis and Evaluation of Dye-Sensitized Solar Cells Made from Zinc Oxide Nanorods

Production of zinc oxide nanostructures in solution phase have attracted wide attentions and triggered various research works aiming at low cost and large scale electrode materials for DSSCs. We have studied the growth of ZnO nanorod array on fluorine-doped tin oxide substrates using a low-temperature solution method. By optimizing the growth parameters, such as reagent concentrations and temperatures (typ. 90 °C), we can control the hydrothermal growth and obtain a maximum length of 18 μm with an aspect ratio of 136. The ZnO nanorods were then applied to the electrode materials of the solar cells. The DSSCs with ZnO nanorods have produced the best energy conversion efficiency η of 1.63%. The effects of the difference in aspect ratio and device process on η have been discussed.

6. Theoretical Investigations on the Adsorption Geometries and Electronic Structures of Azo Dyes Adsorbed on TiO_2

We have employed periodic density functional theory calculations to study the adsorption geometries and electronic structures of azo dyes anchored on TiO_2 surfaces. The theoretical adsorption energies indicate that the bidentate bridging configuration is more preferable than the bidentate chelating and monodentate ester-type geometries. The band gap energies are smaller for the adsorbed complexes than for the clean surfaces, since additional electronic states arise from mixing of the molecular orbitals of the dyes with the TiO_2 valence and conduction bands. The strong electronic coupling between the excited states of azo dyes and conduction bands is observed in the high-efficiency dyes, but not in the low-efficiency dyes. Moreover, the Fermi levels of TiO_2 covered with the former dyes are shifted to higher direction than those with the latter. Thus, the open circuit voltage was increased in DSSCs based on the former dyes.

References

1) H. Katayanagi and K. Mitsuke, *J. Chem. Phys.* **135**, 144307 (8 pages) (2011).
2) H. Katayanagi and K. Mitsuke, *J. Chem. Phys. (Communication)* **133**, 081101 (4 pages) (2010).
3) K. Nakajima, K. Ohta, H. Katayanagi and K. Mitsuke, C*hem. Phys. Lett.* **510**, 228–233 (2011).
4) K. Mitsuke, D. Bashyal and K. Nakajima, *Proc. PACCON* **2011**, 457–460 (2011).

Light Source Developments by Using Relativistic Electron Beams

UVSOR Facility
Division of Advanced Accelerator Research

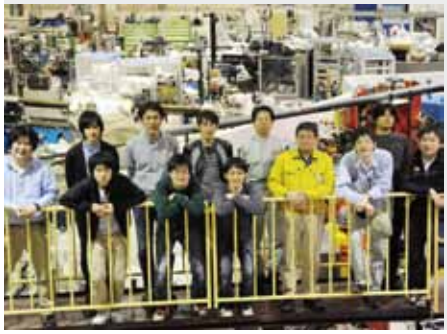

KATOH, Masahiro	Professor
ADACHI, Masahiro	Assistant Professor
ZEN, Heishun	Assistant Professor
TANIKAWA, Takanori	Graduate Student
TAIRA, Yoshitaka	Graduate Student*
KIKUCHI, Yoshitaka	Graduate Student*
GOTO, Yoshiaki	Graduate Student*
WASA, Naoki	Graduate Student*

This project involves researches and developments on synchrotron light source, free electron laser, beam physics and their related technologies. Most of these works are performed at the UVSOR Facility.

1. Developments on UVSOR Accelerators

In these years, we have been preparing for a new injection method called top-up injection at the UVSOR-II electron storage ring.[1)] In this operation scheme, electron beam is re-filled with a short interval, typically one minute, to keep the beam current approximately constant. It was expected that synchrotron radiation experiments under more stable condition would be possible. In July 2010, we have started operating UVSOR-II with the top-up injection fully in the users beam time, which is usually 12 hours a day. The stability of the injection efficiency is essentially important for the stable top-up operation. However, some drifts of the pulse power supplies for the injector and the beam transport system in various time scales, minutes to hours, made the injection efficiency unstable. We have developed a feedback system based on digital oscilloscopes and PC's, and have succeeded to stabilize them.[2)]

In spring 2010, we have installed a new undulator at a straight section created last year by moving the injection point to another short straight section, as shown in Figure 1. The undulator is APPLE-II type and will be used as a modulator in the coherent synchrotron radiation experiments as described later. Another undulator, which will work as a radiator producing coherent harmonic radiation, will be installed in this autumn.

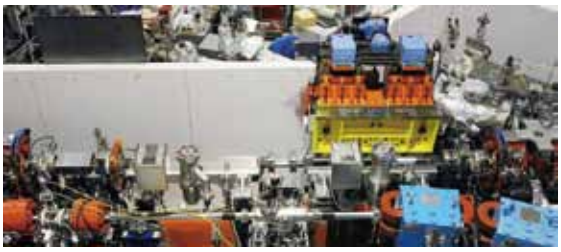

Figure 1. New APPLE-II type undulator just after the installation in spring, 2011. Another undulator will be installed in autumn 2011. Both of them will be used to produce coherent synchrotron radiation.

We have designed a new magnetic lattice for the storage ring, in which the emittance could be reduced by factor of about 2. An upgrade program has been funded based on this design. Eight bending magnets, which have been used for more than 25 years, would be replaced with combined-function ones. The design and construction of new magnets are in progress. A pulse sextupole magnet system was designed and is under construction, which will be used to realize more sophisticated beam injection scheme, in which the electron beam movement during the injection would be reduced significantly not to disturb users experiments. A new 1m long in-vacuum undulator has been designed and is under construction, which will be installed at the last straight section reserved for insertion devices. This upgrade would make UVSOR-II the world brightest low energy synchrotron light source. The reconstruction work would be completed in summer, 2012.

2. Light Source Developments

We have demonstrated that coherent synchrotron radiation of various properties could be generated in an electron storage ring by using an external laser source.[3–5)] This research is supported by the Quantum Beam Technology Program of JST/MEXT. Under this support, a new experimental station is being constructed.[6)] A new undulator was installed. The upgrade of the laser system was completed. Two new beamlines dedicated to the coherent lights in the VUV range and in the THz range is under construction.[7)] The experiments in the new site will be started this winter.

Coherent harmonic generation is a method to produce coherent harmonics of laser light by using relativistic electron beam. We have succeeded in producing the coherent harmonics of Ti:Sa laser in the VUV range, up to 9th harmonic.[8] We observed saturation of the coherent radiation intensity as increasing the laser power. After the saturation, the intensity of the coherent harmonics oscillates with the laser intensity. We have explained this phenomenon as the result of the micro-bunch formation in the over-bunching regime.[9]

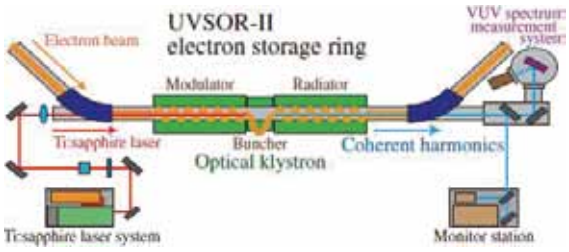

Figure 2. Experimental set-up of Coherent Harmonic Generation at UVSOR-II.

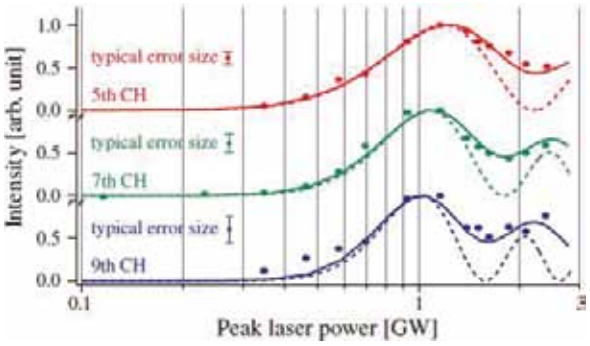

Figure 3. Coherent Harmonic Radiation Intensity vs. Injected Laser Power.

Laser Compton scattering is a technique to produce a quasi-monochromatic X-rays and gamma-rays by using a relativistic electron beam and laser. The laser photons are Compton back-scattered by the high energy electrons and are converted to gamma-rays. The electron beam circulating in the storage ring is very thin in the vertical direction. The typical diameter is in the order of 10 microns. By injecting laser light from the vertical direction to the beam, it is possible to produce ultra-short, quasi-monochromatic, energy tunable, polarization variable gamma-ray pulses. We have already confirmed the tunability of the energy and the polarization.[10] Techniques to measure the pulse width is under development.

3. Developments of Accelerator Technologies

We have observed that operation of the undulators at UVSOR-II affects the beam lifetime and the injection efficiency and sometimes causes problems on the top-up operation. We consider that this is due to the non-linear magnetic field produced by the undulators. To reduce these effects, we are developing multi-wire correction coil system. The coil consists of tens of thin wires on the beam duct at the undulator and produces various correction fields depending on the electric current of each wire. Based on the preliminary experiment last year, we have fabricated a coil with 14 flat wires, in collaboration with Equipment Development Center. It was confirmed that the coil could correct the non-linear field produced by the undulators.[11]

References

1) M. Katoh, M. Adachi, H. Zen, J. Yamazaki, K. Hayashi, A. Mochihashi, M. Shimada and M. Hosaka, *AIP Conf. Proc.* **1234**, 531 (2010).
2) H. Zen, M. Adachi, M. Katoh, K. Hayashi, J. Yamazaki, T. Tanikawa, Y. Taira, M. Hosaka and N. Yamamoto, *Proc. 1st Int. Particle Accel. Conf.* 2576–2578 (2010).
3) (in alphabetic order) S. Bielawski, C. Evain, T. Hara, M. Hosaka, M. Katoh, S. Kimura, A. Mochihashi, M. Shimada, C. Szwaj, T. Takahashi and Y. Takashima, *Nat. Phys.* **4**, 390–393 (2008).
4) M. Labat, M. Hosaka, M. Shimada, M. Katoh and M. E. Couprie, *Phys. Rev. Lett.* **101**, 164803 (2008).
5) M. Shimada, M. Katoh, M. Adachi, T. Tanikawa, S. Kimura, M. Hosaka, N. Yamamoto, Y. Takashima and T. Takahashi, *Phys. Rev. Lett.* **103**, 144802 (2009).
6) M. Adachi, M. Katoh, H. Zen, T. Tanikawa, M. Hosaka, Y. Takashima, N. Yamamoto and Y. Taira, *AIP Conf. Proc.* **1234**, 492 (2010).
7) S. Kimura, E. Nakamura, M. Hosaka, T. Takahashi and M. Katoh, *AIP Conf. Proc.* **1234**, 63 (2010).
8) T. Tanikawa, M. Adachi, M. Katoh, J. Yamazaki, H. Zen, M. Hosaka, Y. Taira and N. Yamamoto, *Proc.1st Int. Particle Acc. Conf.* 2206–2208 (2010).
9) T. Tanikawa, M. Adachi, H. Zen, M. Hosaka, N. Yamamoto, Y. Taira and M. Katoh, *Appl. Phys. Express* **3**, 122702 (3 pages) (2010).
10) Y. Taira, M. Adachi, H. Zen, T. Tanikawa, M. Hosaka, Y. Takashima, N. Yamamoto, K. Soda and M. Katoh, *Nucl. Instrum. Methods Phys. Res., Sect. A* **637**, 5116–5119 (2011).
11) Y. Kikuchi, M. Hosaka, N. Yamamoto, Y. Takashima, M. Adachi, H. Zen and M. Katoh, *UVSOR Activity Report* **2010**, 31 (2011).

* carrying out graduate research on Cooperative Education Program of IMS with Nagoya University

Synchrotron Radiation Spectroscopy on Strongly Correlated Electron Systems

UVSOR Facility
Division of Advanced Solid State Physics

KIMURA, Shin-ichi	Associate Professor
MATSUNAMI, Masaharu	Assistant Professor
MIYAZAKI, Hidetoshi	IMS Fellow*
MORI, Tatsuya	Post-Doctoral Fellow†
IMURA, Keiichiro	Post-Doctoral Fellow
OZKENDIR, Osman Murat	Research Fellow‡
NISHI, Tatsuhiko	Research Fellow§
IIZUKA, Takuya	Graduate Student
HAJIRI, Tetsuya	Graduate Student‖
NIWA, Ryosuke	Graduate Student‖

Solids with strong electron–electron interaction, namely strongly correlated electron systems (SCES), have various physical properties, such as non-BCS superconducting, colossal magneto-resistance, heavy fermion and so on, which cannot be predicted by first-principle band structure calculation. Due to the physical properties, the materials are the candidates of the next generation functional materials. We investigate the mechanism of the physical properties as well as the electronic structure of SCES, especially rare-earth compounds, organic superconductors and transition-metal compounds, by infrared/THz spectroscopy and angle-resolved photoemission spectroscopy based on synchrotron radiation. Since experimental techniques using synchrotron radiation are evolved rapidly, the development of the synchrotron radiation instruments is also one of our research subjects.

1. Electronic-Structure-Driven Magnetic Ordering in a Kondo Semiconductor $CeOs_2Al_{10}$[1,2)]

Cerium-based compounds CeM_2Al_{10} (M = Ru, Os) are new-type of Kondo semiconductors/insulators because they show antiferromagnetic transition at higher temperature than that expected by the Ruderman-Kittel-Kasuya-Yoshida (RKKY) interaction. We reported the anisotropic changes in the electronic structure of a Kondo semiconductor $CeOs_2Al_{10}$ across an anomalous antiferromagnetic ordering temperature (T_0) of 29 K, using optical conductivity spectra as shown in Figsures 1 (a)-(c). The spectra along the a and c axes indicate that an energy gap due to the hybridization between conduction bands and nearly local 4f states, namely the c–f hybridization gap, emerges from a higher temperature continuously across T_0. Along the b axis, on the other hand, another energy gap with a peak at 20 meV becomes visible at 39 K ($> T_0$) and fully opens at T_0 (Figure 1d) because of a charge instability. This result implies that the appearance of the energy gap, as well as the change in the electronic structure along the b axis, induces the antiferromagnetic ordering below T_0.

In the reference material $CeFe_2Al_{10}$, which does not have the anomalous antiferromagnetic ordering, the temperature

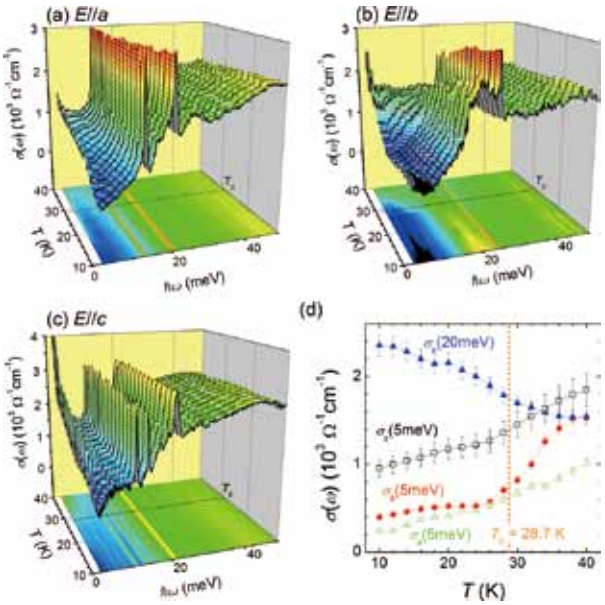

Figure 1. Temperature-dependent optical conductivity [σ(ω)] spectra in E // a (a), E // b (b), and E // c (c) at temperatures from 10 to 40 K. (d) Temperature dependence of representatives of spectral change. σ_x(5 meV) [x = a, b, c (x is axis name)] and σ_b(20 meV) are the intensities of the σ(ω) spectra at 5 and 20 meV, respectively.

dependence of the polarized optical conductivity [σ(ω)] spectra were also reported. The σ(ω) spectrum along the *b*-axis differs greatly from that in the *ac*-plane, indicating that this material has an anisotropic electronic structure. At low temperatures, in all axes, a shoulder structure due to the optical transition across the hybridization gap between the conduction band and the localized 4f states, namely c–f hybridization, appears at 55 meV. However, the gap opening temperature and the temperature of appearance of the quasiparticle Drude weight are strongly anisotropic indicating the anisotropic Kondo effect. The strong anisotropic nature in both electronic structure and Kondo effect is considered to be relevant to the anomalous magnetic phase transition in $CeRu_2Al_{10}$ and $CeOs_2Al_{10}$.

2. Nodeless Superconducting Gap in $A_xFe_2Se_2$ (A = K, Cs) Revealed by Angle-Resolved Photoemission Spectroscopy[3)]

Pairing symmetry is a fundamental property that characterizes a superconductor. For the iron-based high-temperature superconductors, an $s_{\pm}$-wave pairing symmetry has received increasing experimental and theoretical support. More specifically, the superconducting order parameter is an isotropic s-wave type around a particular Fermi surface, but it has opposite signs between the hole Fermi surfaces at the zone center and the electron Fermi surfaces at the zone corners. Here we report the low-energy electronic structure of the newly discovered superconductors, $A_xFe_2Se_2$ (A = K, Cs) with a superconducting transition temperature (T_c) of about 30 K. We found $A_xFe_2Se_2$ (A = K, Cs) is the most heavily electron-doped among all iron-based superconductors. Large electron Fermi surfaces are observed around the zone corners as shown in Figure 2, with an almost isotropic superconducting gap of ~10.3 meV, whereas there is no hole Fermi surface near the zone center, which demonstrates that interband scattering or Fermi surface nesting is not a necessary ingredient for the unconventional superconductivity in iron-based superconductors. Thus, the sign change in the $s_{\pm}$ pairing symmetry driven by the interband scattering as suggested in many weak coupling theories becomes conceptually irrelevant in describing the superconducting state here. A more conventional s-wave pairing is probably a better description.

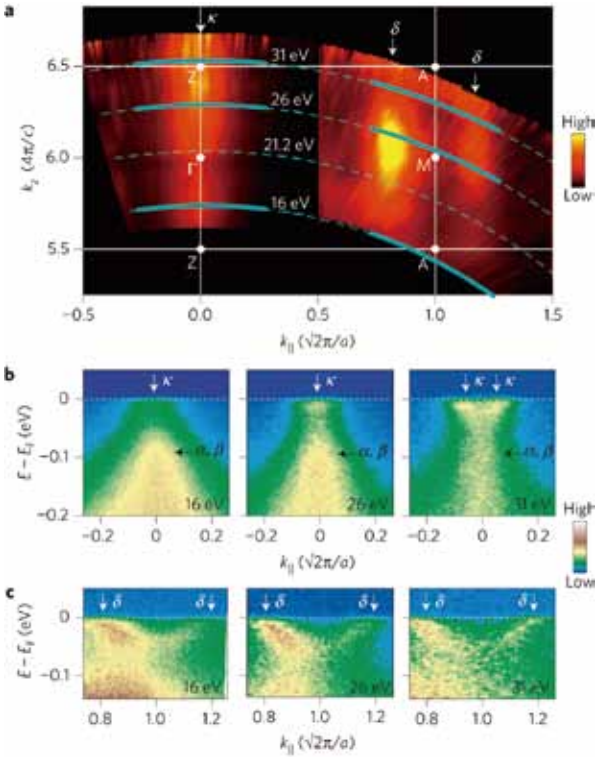

Figure 2. The photoemission intensity of $K_{0.8}Fe_2Se_2$ in the ΓZAM plane. The intensity was integrated over a window of (E_F–15 meV, E_F+15 meV). Different k_z's were accessed by varying the photon energy at Beamline 7U of UVSOR, as indicated by the dashed lines, where an inner potential of 11 eV is used to obtain k_z. **b**, **c**, Photoemission intensity along the three momentum cuts across Γ–Z, and the other three momentum cuts across M–A respectively as marked by thick solid lines in **a**. The data were taken with horizontally polarized 16, 26 and 31 eV photons.

References

1) S. Kimura, T. Iizuka, H. Miyazaki, A. Irizawa, Y. Muro and T. Takabatake, *Phys. Rev. Lett.* **106**, 056404 (2011).
2) S. Kimura, Y. Muro and T. Takabatake, *J. Phys. Soc. Jpn.* **80**, 033702 (2011).
3) Y. Zhang, L. X. Yang, M. Xu, Z. R. Ye, F. Chen, C. He, H. C. Xu, J. Jiang, B. P. Xie, J. J. Ying, X. F. Wang, X. H. Chen, Jiangping Hu, M. Matsunami, S. Kimura and D. L. Feng, *Nat. Mater.* **10**, 273 (2011).

* Present Address; Center for Fostering Young and Innovative Researchers, Nagoya Institute of Technology
† Present Address; Graduate School of Pure and Applied Sciences, University of Tsukuba
‡ from Mersin University, Turkey
§ from Chiba University
|| carrying out graduate research on Cooperative Education Program of IMS with Nagoya University

Electronic Structure and Decay Dynamics in Atoms and Molecules Following Core Hole Creation

UVSOR Facility
Division of Advanced Photochemistry

SHIGEMASA, Eiji — Associate Professor
IWAYAMA, Hiroshi — Assistant Professor
ISHIKAWA, Lisa — Post-Doctoral Fellow

The dynamics of the inner-shell photoexcitation, photoionization, and subsequent decay processes is much more complex, in comparison to outer-shell photo-processes. For instance, the inner-shell photoionization is concomitant with the excitation and ionization of valence electrons, which reveal themselves as shake-up and shake-off satellite structures in the corresponding photoelectron spectrum. The one-photon multi-electron processes, which are entirely due to the electron correlation in the system, are known to happen not only in the primary inner-shell hole creation processes, but also in their relaxation processes. Our research project is focused on elucidating the electronic structures and decay dynamics in core-excited atoms and molecules, by utilizing various spectroscopic techniques together with monochromatized synchrotron radiation in the soft x-ray region.

1. Doppler Effect in Fragment Autoionization Following Core-to-Valence Excitations

The Doppler effect is known to occur when the source and observer are in motion relative to each other, leading to an apparent change in the observed frequency of the propagating wave. This effect has a wide variety of applications in many fields, relating to the sensing of movement. In the research field of molecular science, the sensing of nuclear motion has long been an attractive issue. Gel'mukhanov and co-workers predicted in 1998[1] that the nuclear motion in 'ultrafast dissociation' following molecular core-level photoexcitation can be probed by the Doppler effect in emitted Auger electron. Ultrafast dissociation is a process where the molecular dissociation at the core-excited state precedes the Auger decay and then an atomic fragment emits an Auger electron. This atomic Auger electron can possess the opposite Doppler shift depending on the direction approaching the detector (label (A) in Figure 1(a)) or moving away from it (label (B) in Figure 1(a)). This electron Doppler shift in kinetic energy can be expressed as $\mathbf{p}\cdot\mathbf{v}$, where $\mathbf{p}$ is the momentum of the electron and $\mathbf{v}$ is the velocity vector of the emitting fragment, and thus it becomes maximum when both vectors are parallel. Although molecules in the gas phase are randomly oriented, molecular photoabsorption is known to be highly anisotropic relative to the polarization vector of the incident radiation. Therefore, detection of the emitted Auger electron along the preferred direction of emission of the fragment makes the measurement of the Doppler shift possible experimentally.

In our recent works,[2] it has been disclosed that the Doppler effect can be utilized as a unique tool to investigate the molecular dynamics at singly-charged ion states produced by resonant Auger decay. Special attention is paid to detecting slow electrons. In cascade Auger decay, two electrons are ejected sequentially with distinct kinetic energies depending on the energy levels of the initial, intermediate, and final electronic states involved. One of the two emitted electrons is often slow (typically less than 5 eV). Singly-charged molecular ion states populated by the first electron emission can undergo competition between second electron emission and molecular dissociation. If one of the dissociating fragments is excited it may subsequently autoionize; the autoionizing atomic fragment can act as an electron emitter which can exhibit a Doppler splitting if the kinetic energy of the atomic fragment is sufficiently large and the initial photoabsorption anisotropy is substantially maintained in the angular distribution of fragments.

As an example, the O* autoionizing electron spectrum following the O1s $\rightarrow \sigma^*$ excitation in O_2 is denoted in Figure 1(b). Clear Doppler profiles, depending on the fragment-ion directions as labeled in (A) or (B), are discernable in the atomic oxygen autoionization peaks. The corresponding Doppler

profiles, as a counterpart of the fragmentation process, are also seen in the atomic Auger electron peak. It is clarified that femtosecond dissociation dynamics of singly-charged ion states produced by resonant Auger decay can be deduced from the information obtained by analyzing the Doppler profiles. In the cascade Auger decay following the O1s → σ* excitation in O_2, it is concluded that the slow Auger electrons are produced by autoionization of valence-excited atomic fragments created simultaneously to the core-excited atomic fragments during ultrafast dissociation of the oxygen molecule.

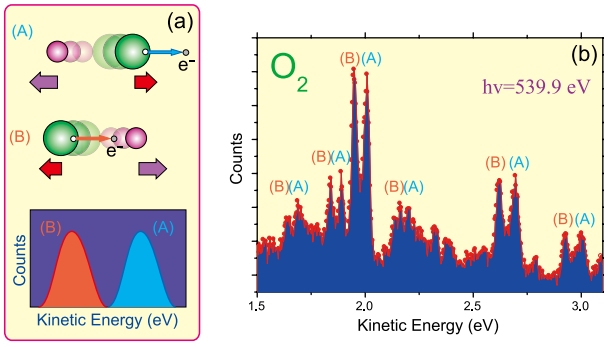

Figure 1. (a) Schematic representations for explaining a source of the electron Doppler splittings in kinetic energy, and (b) Doppler splittings observed in the autoionizing electron spectrum from an atomic oxygen following the O1s → σ* excitation in O_2.

2. Two-Dimensional Electron Spectroscopy on BL6U

A new project for constructing the undulator beamline BL6U has been initiated since 2007. A Monk-Gillieson mounting with a variable-included-angle mechanism has been chosen, in order to cover a wide photon energy region (30–500 eV) with one single grating. It has been confirmed through its performance tests that the monochromator designed can cover the photon energy ranging from 40 to 400 eV with the resolving power higher than 5000 and the photon flux more than 10^{11} photons/sec, when the storage ring is operated in the top-up mode.

A new electron spectrometer, MBS-A1, for gas phase spectroscopy has successfully been installed, in parallel with the construction program of BL6U. High-resolution electron spectroscopy is a powerful method to study electronic structures of atoms and molecules, especially when high-resolution electron spectra and their polarization dependences are measured as a function of photon energy. The ability of this two dimensional (2D) electron spectroscopy has been proved in our recent work at SPring-8.[2,4] In order to apply high-resolution 2D electron spectroscopy to the investigation of the L-shell excitations of the second row elements, a new experimental setup for BL6U has been designed and constructed.

For realizing 2D electron spectroscopy with high resolution, software development for controlling both the beamline monochromator and MBS-A1 analyzer has been performed. For the beamline monochromator, not only its output but the gap of the undulator should be controlled. After careful optimizations for the undulator gaps, 2D electron spectroscopy on BL6U has become feasible, thanks to the stable operation of the UVSOR-II storage ring.

Figure 2 demonstrates the 2D maps for the de-excitation spectra following the double excitations near the carbon 1s photoionization threshold in CO, measured in (a) horizontal, and (b) vertical directions, respectively, as an example of successful measurements. The exit slit opening of the monochromator was set at 30 μm, which corresponds to the photon energy resolution of about 60 meV. The pass energy and slit width of the MBS-A1 analyzer were set to 100 eV and 0.2 mm, which results in the electron energy resolution of about 60 meV. The straight lines with a slope of 1 in the high kinetic energy (KE) region in each 2D map are due to the valence photoelectrons with vibrational structures. The vertical lines around KE of 275 eV in Figure 2(b) are assigned to the atomic Auger line from oxygen atoms after the dissociation of CO molecules. Some island-like structures are seen in the KE range of 267–270 eV in Figure 2(a) and Figure 2(b), which seem to be specific to the decay processes of the double excitations. The complicated photon energy dependences of the structures may suggest that the de-excitation processes of the doubly excited states of CO are not so simple.

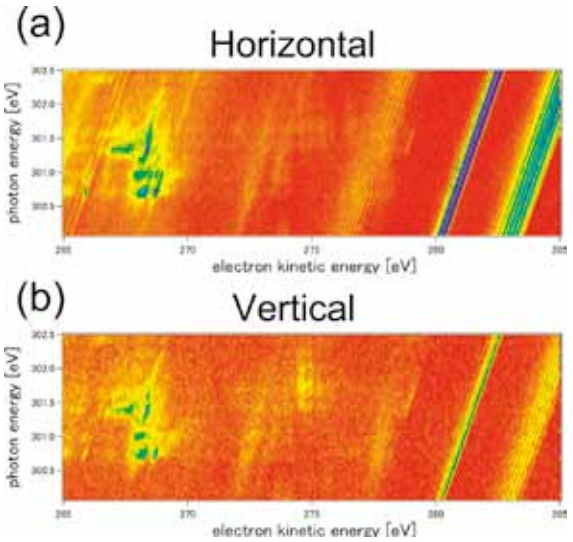

Figure 2. 2D map of de-excitation spectra following the double excitations around the carbon K-edge of CO, measured in (a) horizontal, and (b) vertical directions, respectively.

References

1) F. Gel'mukhanov, H. Ågren and P. Sałek, *Phys. Rev. A* **57**, 2511–2526 (1998).
2) E. Shigemasa *et al.*, *New J. Phys.* **12**, 063030 (9 pages) (2010).
3) R. Guillemin *et al.*, *Phys. Rev. A* **82**, 051401(R) (4 pages) (2010).
4) T. Kaneyasu *et al.*, *Phys. Rev. Lett.* **101**, 183003 (4 pages) (2008).

Micro Solid-State Photonics

Laser Research Center for Molecular Science
Division of Advanced Laser Development

TAIRA, Takunori	Associate Professor
LOISEAU, Pascal	Visiting Associate Professor
ISHIZUKI, Hideki	Assistant Professor
AKIYAMA, Jun	IMS Research Assistant Professor
TSUNEKANE, Masaki	Post-Doctoral Fellow
SATO, Yoichi	Post-Doctoral Fellow
JOLY, Simon	Post-Doctoral Fellow
BHANDARI, Rakesh	Post-Doctoral Fellow
KONG, Weipeng	Graduate Student
ITO, Yuta	Graduate Student*
ONO, Yoko	Secretary
INAGAKI, Yayoi	Secretary

The artistic optical devices should be compact, reliable, efficient and high power light sources. With the approaches of domain structures and boundaries engineering, it is possible to bring the new interaction in their coherent radiation. The high-brightness nature of Yb or Nd doped single crystal or ceramic microchip lasers can realize efficient nonlinear wavelength conversion. In addition, designed nonlinear polarization under coherent length level allows us new function, such as the quasi phase matching (QPM). The development of "***Micro Solid-State Photonics***," which is based on the micro domain structure and boundary controlled materials, opens new horizon in the laser science.

1. Composite, All-Ceramics, High-Peak Power Nd:YAG/Cr^{4+}:YAG Monolithic Micro-Laser with Three-Beam Output for Engine Ignition

A passively Q-switched Nd:YAG/Cr^{4+}:YAG micro-laser with three-beam output was realized for multi-point ignition of an automobile engine as shown in Figure 1. A single active laser source made of a composite, all-ceramics Nd:YAG/Cr^{4+}:YAG monolithic cavity with a length of 10 mm was pumped by three independent lines. At 5 Hz repetition rate, each line delivered laser pulses with energy of 2.4 mJ and 850-ps pulse duration (2.8-MW peak power). The M^2 factor of a laser beam was 3.7, and stable air breakdowns were realized. The increase of pump repetition rate up to 100 Hz improved the laser pulse energy by 3% and required an increase of the pump pulse energy by only 5%. We confirmed that pulse timing of the laser-array beams could by adjusted by less than 5% tuning of an individual line pump energy, and then simultaneous multi-point ignition is possible.

Figure 1. Microchip laser with three-beam output.

2. Development of Megawatt-Peak-Power UV Microchip Laser

Megawatt peak power, giant pulse microchip lasers are attractive for wavelength conversion, provided their output is linearly polarized. We use a [110] cut Cr^{4+}:YAG for passively Q-switched Nd:YAG microchip laser to obtain a stable, linearly polarized output. Then, we optimize the conditions for second harmonic generation (SHG) using Lithium Triborate (LBO) to achieve > 6 MW peak power, 1.7 mJ, 265 ps, 100 Hz pulses at 532 nm wavelength with a conversion efficiency of 84.71%. Further, using β-Barium Borate (BBO) for fourth harmonic generation (FHG), we obtain > 2 MW peak power, 562 μJ, 260 ps, 100 Hz pulses at 266nm with 51.2% conversion efficiency as shown in Figure 2. These are world records for SHG and FHG using microchip lasers.

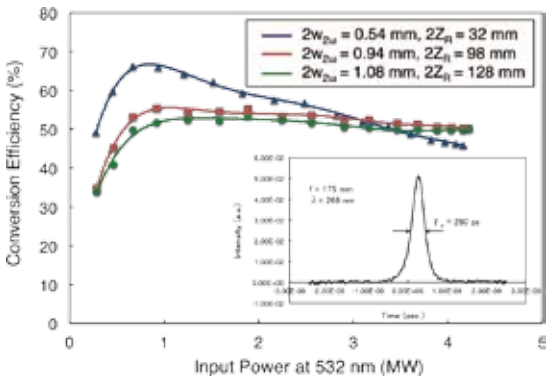

Figure 2. FHG conversion characteristics under different focusing conditions.

3. Variation of the Stimulated Emission Cross Section in Nd:YAG Caused by the Structural Changes of Russell-Saunders Manifolds

It was experimentally found that electronic structures of Russell-Saunders manifolds in Nd:YAG depended on the Nd^{3+}-doping concentration (C_{Nd}) and its fabrication process. Both of the bandwidth and the branching ratio in fluorescent transitions in Nd:YAG varied almost linearly depending on C_{Nd}, and a fabrication process has its own diluted limit of the bandwidth and the branching ratio. Also dependences of Stark splitting in Nd:YAG were also observed. As a result, Nd^{3+}-doping causes 1.9% and 4.5% reduction in the maximum value of the stimulated emission cross section (σ) of Nd:YAG per 1 at.% of C_{Nd} at 1.064 μm and 1.319 μm, respectively. Figure 3 shows the concentration dependence of σ in Nd:YAG at 1.064-μm (a) and 1.319-μm (b).

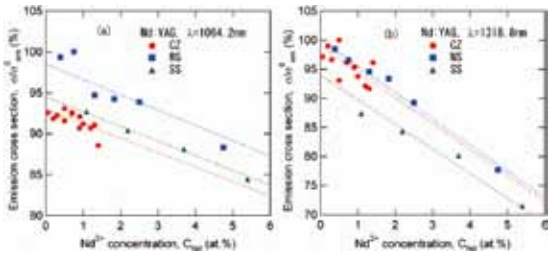

Figure 3. The ratio between σ to the Nd^{3+}-diluted limit ($\sigma_{em}{}^0$) of Nd:YAG at 1.064-μm (a) and 1.319-μm (b). Circle, triangle, and square indicate $\sigma/\sigma_{em}{}^0$ of CZ, SS, and WS, respectively.

4. Demonstration of Rare-Earth-Doped Anisotropic Ceramic Laser

We succeeded in developing a QCW-diode-pumped "anisotropic ceramic laser" by using micro-domain-controlled neodymium doped hexagonal fluorapatite [Nd_3:$Ca_{10}(PO_4)_6F_2$, Nd:FAP] polycrystalline ceramics as the gain medium, which were fabricated by the rare earth assisted magnetic grain-orientation control method, as a step toward achieving giant micro photonics. The laser delivers 1063.10 and 1063.22 nm output beams when pumped with a central wavelength of 807.5 nm and a 2 nm bandwidth diode laser operating in quasi-continuous-wave (QCW) mode. The resulting slope efficiency with respect to the absorbed power was 2.6% and the oscillation threshold was 12 W when uncoated 2 at.% Nd:FAP material was used as Figure 4.

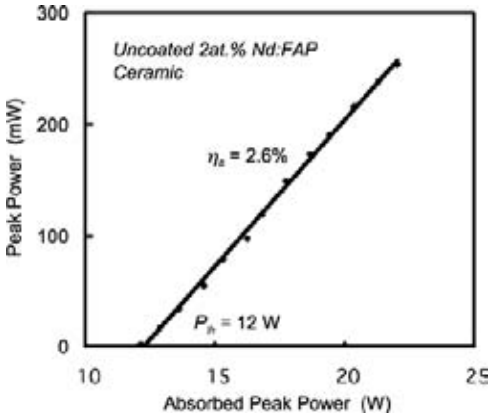

Figure 4. Nd:FAP QCW peak laser output power at 1.06 μm *versus* pump power at 807.5 nm. The pump pulse duration and repetition rate are 420 μs and 6 Hz.

5. PFabrication of Slant Quasi-Phase Matching Structure in Mg-Doped Congruent $LiNbO_3$

We fabricated slant quasi-phase-matching structure in 2-mm-thick Mg-doped $LiNbO_3$ crystal at 65° slant angle with 75-μm surface period as Figure 5. Slant QPM has a possibility of wafer-scale-aperture device, suitable for handling high power/energy lasers.

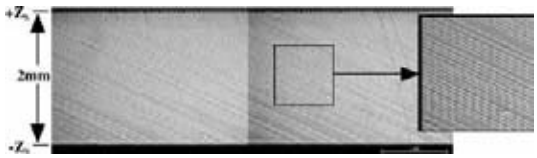

Figure 5. Y-face photograph of obtained slant QPM structure in 65° slant MgLN with thickness d_1 = 2 mm. Surface QPM period Λ_1 = 75 μm.

References

1) N. Pavel, M. Tsunekane and T. Taira, *Opt. Express* **19**, 9378–9384 (2011).
2) R. Bhandari and T. Taira, T*echnical Digest of Nonlinear Optics 2011 (NLO2011)*, NME2, Kauai, Hawaii, USA (July 17–22, 2011).
3) Y. Sato and T. Taira, *Opt. Mater. Express* **1**, 514 (2011).
4) J. Akiyama, Y. Sato and T. Taira, *Appl. Phys. Express* **4**, 022703 (2011).
5) H. Ishizuki and T. Taira, *Technical Digest of Nonlinear Optics (NLO2011)*, NMA4, Kauai, Hawaii, USA (July, 17–22, 2011).

* carrying out graduate research on Cooperative Education Program of IMS with Ibaraki University.

Ultrafast Laser Science

Laser Research Center for Molecular Science
Division of Advanced Laser Development

FUJI, Takao	Associate Professor
NOMURA, Yutaka	Assistant Professor
MASUDA, Michiko	Secretary
KAWAI, Shigeko	Secretary

Speed of ultrafast energy transfer from light to molecules (*i.e.* primary processes of photosynthesis, photoisomerization in visual pigments, *etc.*) is on the order of femtosecond (10^{-15} s). In our laboratory, we develop cutting edge lasers for such ultrafast molecular science, namely, femtosecond or attosecond (10^{-18} s) ultrashort pulse lasers.

For example, arbitrary waveform synthesis can be performed with simultaneous generation of femtosecond light pulses in various wavelength regions and superimposition of them with precisely controlled phases.

We would like to develop such advanced light control technology, which can push forward the research on ultrafast photochemical reactions.

1. Ultrabroadband Mid-Infared Source Based on Four-Wave Rectification[1)]

Optical rectification is one of the most commonly used frequency conversion processes for generation of ultrashort teraherz wave. The nonlinear process basically produces a wave whose shape is proportional to a derivative of temporal intensity profile of an input pulse.

Nowadays 7-fs Ti:Sapphire oscillators are commercially available, thus by using such a light source it is even possible to generate broadband mid-infrared light through the optical rectification assuming perfect phase matching condition. Comparing with a traditional mid-infrared ultrashort pulse generation with sequential down conversion processes, the most unique feature of the scheme is that carrier-envelope phase of the generated mid-infrared pulses is passively stabilized.

Several groups demonstrated such broadband and phase-stable light generation with solid nonlinear crystals. However, it is not realistic to have broadband spectrum which covers the entire mid-infrared (3–20 μm) region by using nonlinear solid crystals because of the limited transmission bandwidth.

On the other hand, optical rectification with gas media is an interesting alternative technique since transmission bandwidth of gases is much wider than that of solid media. In fact, rare gases are completely transparent from teraherz to visible region. Although the largest drawback of gas media is low nonlinear coefficient, it is possible to use much more intense pumping pulse than that for solid media, and filamentation effect of ultrashort pump pulses can enhance the efficiency of the frequency conversion.

Ultrabroadband mid-infrared pulse generation through the optical rectification (four-wave rectification) in gases was firstly demonstrated in 2007,[2)] and the technique was followed by several groups. Such mid-infrared pulses with more than one octave at full width at half maximum are very attractive to be applied for molecular spectroscopy, *e.g.* two-dimensional infrared spectroscopy.

Here, latest progress of the mid-infrared pulse generation by four-wave rectification through filamentation in gases and the detailed characterization of the generated mid-infrared pulses are to be shown. In addition, we performed three-dimensional (3D) numerical simulation and compared the

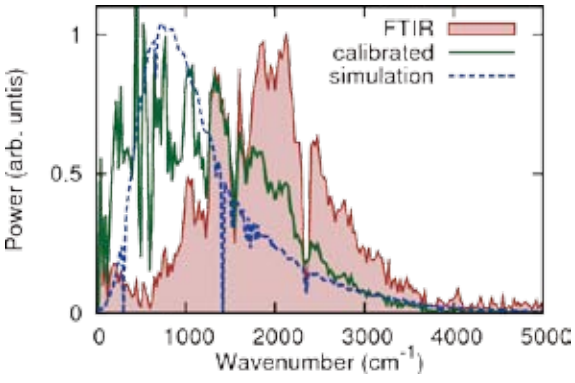

Figure 1. A typical spectrum of the mid-infrared pulse generated through the four-wave rectification process (filled curve, Brown). The spectrum was measured with a home-built Fourier transform infrared spectrometer. Sharp dips at 2400 cm^{-1} and at around 1800 cm^{-1} are due to absorption of carbon dioxide and water vapor in air, respectively. The solid line (Green) shows a spectrum after sensitivity calibration. The dotted line (Blue) shows a spectrum obtained from three-dimensional numerical simulation. The scale of the vertical axis is linear.

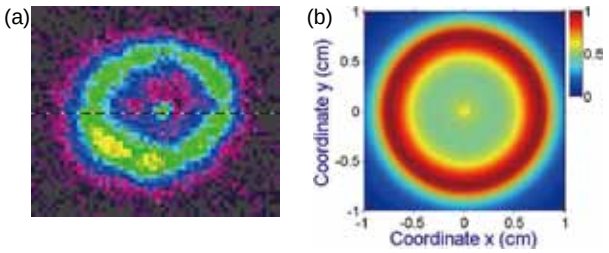

Figure 2. (a) Experimental and (b) simulated radical intensity distributions of the mid-infrared pulses.

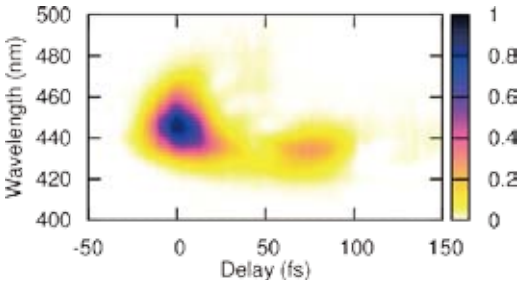

Figure 3. Measured XFROG trace.

experimental and theoretical results.

The light source was based on Ti:Sapphire multi-pass amplifier system (800 nm, 25 fs, 800 μJ@1 kHz). The second harmonic (ω_2, 90 μJ) and the fundamental (ω_1, 600 μJ) were spatially and temporally overlapped and focused into air by a concave mirror (r = –500 mm). A plasma column with a length of ~2 cm appeared around the focus. The mid-infrared pulse (ω_0) generated through four-wave rectification process ($\omega_1 + \omega_1 - \omega_2 \rightarrow \omega_0$) was filtered through Si and Ge plates and was introduced into a home-built fourier transform spectrometer. The Michelson-type interferometer consisted of a Ge coated KBr beam splitter, sliver mirrors, a feedback loop translation stage with 5 nm resolution, and a TGS (triglycine sulfate) pyroelectric detector.

The measured spectrum is shown as a filled curve (Brown) in the Figure 1. The broadband spectrum, which spread in whole mid-infrared region (500–4000 cm^{-1}), was generated due to broadband phase matching through the low dispersive gas medium. The power spectrum calibrated by using a SiC lamp (80007, Oriel) with known color temperature is also shown as a solid curve (Green) in Figure 1. Although the power in the frequency region lower than 500 cm^{-1} is not so reliable since the beam splitter in the Michelson-type interferometer was designed for > 500 cm^{-1}, it is very likely that the generated spectrum has significant intensity in the low frequency region. The pulse energy of the mid-infrared pulse was measured as ~250 nJ by using a pyroelectric detector (J-10MB-LE, Coherent). With this energy level, it is possible to apply the pulses for nonlinear spectroscopy for condensed matter. The pulse-to-pulse intensity fluctuation was about 2.5% rms. The transform-limited pulse calculated from the calibrated spectrum has less than 10 fs pulse duration, which is less than half the period of the center frequency (~1500 cm^{-1}). The passively stabilized carrier-envelope phase owing to the optical rectification scheme is highly valuable for the half-cycle pulses.

To explain the extremely broad spectrum, we performed a 3D modeling of nonlinear optical transformation of a high-intensity two-color field in air at atmospheric pressure. Our model is based on the slowly evolving wave approximation modified to include ionization of the gas by ultrashort laser pulses. The nonlinear polarization term includes not only the $\omega_1 + \omega_1 - \omega_2 \rightarrow \omega_0$ term, but all possible four-wave mixing terms, including those describing self- and cross-phase modulation and third-harmonic generation. Simulations were performed in parallel codes on the Lomonosov supercomputer facility at Moscow State University. The simulated spectrum is shown as a dashed curve (Blue) in Figure 1.

Characterization of the beam profile and the angular dispersion are important for further application of the light source. We have measured the beam profile of the infrared beam by using a pyroelectric camera (Pyrocam III, Spiricon). The measured beam profile is shown in Figure 2(a). The shape of the beam was ring, which seems to correspond to conical emission of the filament. Angle of the cone was estimated to be about 3 deg.

Figure 2(b) shows the simulated beam profile of the mid-infrared pulse obtained from the 3D simulation at the same time as the spectrum. The ring shape and the angle of the cone were well reproduced. Standard phase matching for the relevant four-wave mixing process does not explain the conical emission pattern. The pattern is accurately reproduced in our simulations only when the full ionization-assisted coupled dynamics of optical fields involved in the generation of mid-infrared ultrashort waveforms is included in the analysis. According to the simulation, the conical emission does not have significant angular dispersion, then it should be possible to compress the pulse down to single cycle.

To quantitatively evaluate the temporal shape of the generated infrared pulse, we measured cross-correlation frequency resolved optical gating (XFROG). A small portion of the fundamental (ω_1) 25 fs pulse was used as a reference pulse. The reference pulse and the infrared pulse (ω_0, test pulse) were focused into air with a off-axis parabolic mirror (f = 150 mm). Generated four-wave mixing spectra ($\omega_1 + \omega_1 - \omega_0 \rightarrow \omega_2$) were measured with a spectrometer (USB2000+, Ocean Optics) by scanning the delay time between the reference pulse and the infrared test pulse.

The measured XFROG trace is shown in Figure 3. The pulse width was estimated to be 15 fs, which is 1.1 cycles for 4.2 μm carrier wavelength, from a retrieved temporal profile of the test pulse (FROG error was ~0.4%). The result clearly indicates that the generated MIR spectrum is coherent.

References

1) T. Fuji and Y. Nomura, *20th International Laser Physics Workshop (LPHYS'11)*, 5.3.4 Sarajevo, July 11–15 (2011). (invited talk)

2) T. Fuji and T. Suzuki, *Opt. Lett.* **32**, 3330–3332 (2007).

Visiting Professors

Visiting Professor
KODAMA, Ryosuke *(from Osaka University)*

High Energy Density Sciences

Now it is relatively easy to realize high energy density states with high power lasers. The states would have a variety of attractive fields of sciences and technologies such as particle acceleration, laboratory astrophysics, and material science, nuclear science including medical applications and laser fusion, which is "High Energy Density Science: HEDS." One of the advantages of the HED states is its energy density, which is much higher than that of the solid state matter. He is now exploring high energy density sciences in methods of introducing a Plasma Photonics concept to control intense light and high energy charged particles with high energy density plasmas. Nonlinear interaction of intense light with vacuum or nonlinear optics in vacuum will be significantly enhanced with the focusing angle of the interaction laser light, which must be realized by applying the novel geometry with plasma photonic devices. As his other important topics, he is interested in creation of high pressure condensed matter such as metallic solid hydrogen with high power lasers. Freezing of a higher energy density state or metallic Si have been already realized, extending the new scheme to more number of materials to have novel materials in hand, which have never seen on the earth.

Visiting Professor
KONDOH, Hiroshi *(from Keio University)*

Surface Dynamic Processes Studied by Soft X-Ray Spectroscopy

We have been working on surface dynamic processes such as charge transfer from a molecule to a substrate and surface catalytic reactions using synchrotron-based soft x-ray spectroscopies. Recently we have studied the time scale of the charge transfer from organic molecules to metal substrates by means of the core-hole decay spectroscopy. For instance, the Coster-Kronig autoionization accompanying the S 2s–3p transition was used for estimation of the time constant for the charge transfer from a sulfur-containing molecule to a metal substrate at BL-6U in the UVSORII. The resultant time constant were found to be of the order of sub-femtosecond. Another research subject regarding the surface dynamic process is the understanding of surface catalytic process which proceeds under ambient pressure conditions. In particular, applying the soft x-ray absorption spectroscopy with the transmission mode to real-time observation of catalytic processes will allow us to understand the reaction mechanism under the practical working condition of the catalyst.

Visiting Associate Professor
UENO, Kosei *(from Hokkaido University)*

Near-Field Intensity Profile of Metallic Nanostructures Using Near-Field Optical Microscope

The global problems relevant to the environment and energy are attracting attention, so that it is considered that the construction of efficient light-energy conversion devices serves as an important subject of the scientific research. Thus far, the interaction between photons and molecules has not received much attention in photochemistry. However, the creation of a progressive methodology that allows an increase in the excitation probability is necessary. Namely, to create a low-carbon-emitting society by utilizing light energy, it is necessary to introduce the concept of "effective utilization of photons" to photochemistry. We develop photochemical reaction fields, in which make it possible to increase the interaction between photons and molecules. Metallic nanostructures showing localized surface plasmon resonance are a promising approach for the development of photochemical reaction fields. Therefore, we study the optical properties of the metallic nanostructures which are prepared with nanometric accuracy and elucidate its near-field intensity profile according to using a near-field optical microscope developed by Prof. Okamoto in IMS to investigate fundamental mechanisms of the concept of "effective utilization of photons" induced by metallic nanostructures.

Visiting Associate Professor
TAKAHASHI, Toshiharu *(from Kyoto University)*

Development of New Spectroscopic Methods Using THz Coherent Synchrotron Radiation

We are developing new spectroscopic techniques with coherent synchrotron radiation (CSR) in the THz-wave region. One is the technique of the scanning near-field transmission and reflection microscopy using broadband CSR, where the high spatial resolution below the diffraction limit is available. Second, the method of the monochromatic THz-wave pump–photoemission probe spectroscopy (PES) is also developing. Since the VUV radiation by the coherent harmonic generation (CHG) can be emitted using the laser pulse in UVSOR, the jitter-free pump-probe spectroscopy is possible with the THz-CSR. In order to perform these spectroscopic techniques, we are constructing a new CSR beamline (BL1B) in UVSOR.